

Measurement of Gas Condensate Relative Permeabilities utilizing NMR and MRI Technologies

Michael Rauschhuber^{1,*}, Jon Burger¹, Josephina Schembre-McCabe¹, Elton Yang¹, and Boqin Sun¹

¹Chevron Technical Center, Chevron, U.S.A Inc., Houston, TX, USA

Abstract. During the production of gas condensate reservoirs, the reservoir pressure is reduced to below the dewpoint, causing retrograde condensation and reduction in gas relative permeability. Prediction of deliverability in these fields requires sets of relative permeability measurements at different capillary numbers. The experimental study consisted of measurements of gas condensate relative permeabilities utilizing pseudo steady state core floods and a synthetic gas condensate mixture of heptane and methane with a dew point of 3,750 psia and a condensate-to-gas ratio (CGR) of 80 STB/MMSCF. The testing covered various lithologies, limestone, tight sandstone, and various shale samples. Single phase permeability was measured above the dew point followed by gas and condensate relative permeability measurements at multiple pressure steps below the dew point. At each pressure step, multiple flow rates were incorporated to span several orders of magnitude of capillary number. Their single-phase gas condensate -permeabilities spanned from 52 mD to $4 \cdot 10^{-4}$ mD allowing superficial velocities to span multiple orders of magnitude, and thus the capillary number to range from 10^{-2} to 10^{-10} . To determine saturation more accurately, Nuclear Magnetic Resonance (NMR) and Magnetic Resonance Imaging (MRI) were incorporated into core flooding rigs. Two separate systems were utilized. The first system included a 2 MHz Magritek spectrometer, and the second, a 42 MHz Aspect Imaging MRI. T_1 - T_2 measurements and/or MRI-SPRITE measurements were employed for in-situ measurements of saturations at various pressure steps throughout the core floods. The results obtained in this study enrich the database of gas condensate relative permeability and increases our understanding of the effects of the pore systems on the gas condensate flow in porous media.

1 Introduction

Liquid drop out during pressure depletion of a retrograde gas condensate reservoir may restrict gas flow and reduce well deliverability [1]. Under the dew point pressure, the reservoir behaviour is complex with two competing mechanisms, resulting in effective gas permeabilities to be rate-dependent. This phenomena is modeled as a function of the capillary number [2]. While near well bore impairment is mainly in the regime of high capillary numbers, widespread interest in tighter and less permeable formation drives the concern in understanding the behavior of gas condensates systems to smaller capillary numbers, a regime dominated by interfacial phenomena similar to rich gases flowing through a shale matrix.

In this work, we present the results of an experimental study combining coreflood and Nuclear Magnetic Resonance (NMR) and/or Magnetic Resonance Imaging (MRI) to understand the impacts of the flow of gas condensates through porous systems. Experimental coreflood data is used to determine condensate and gas relative permeabilities over a broad range of capillary numbers. NMR and MRI are robust technologies applied in petrophysical and core analysis evaluations [3]. Here, we combine in-situ with the coreflood apparatus to yield a better understanding of fluid saturation during the displacement.

2 Experimental Methods

2.1 Coreflood Setup

Pseudo-steady state corefloods were conducted to determine relative permeabilities [4]. Two apparatus were built (figure 1). The first utilized a low field 2 MHz Magritek Rock Analyzer, and the second unit employed a 42 MHz Aspect M12 MRI Imager with custom probe and gradient set from Doty Scientific. Zirconia coreholders from Daedalus Innovations enabled the core flooding rigs to be NMR/MRI compatible.

Core samples were selected from a range of lithologies, including a limestone, a tight sandstone, and three shale samples. Experiments were performed in an as-received state. Effective permeabilities to single phase gas condensate were measured, and porosity determined via NMR. Samples cover a broad range of permeabilities spanning from 50 mD to $2 \cdot 10^{-4}$ mD. Table 1 provides a summary of the core properties. Samples ranged in length from 25 (Sample A) to 52 mm (ILS). Probes used in both the 2 MHz spectrometer and

* Corresponding author: mrauschhuber@chevron.com

42 MHz Imager are capable of measuring samples up to 60 mm in length.

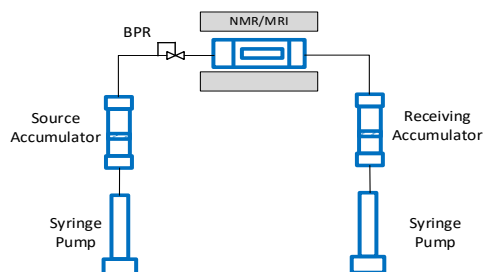


Fig. 1. Schematic of coreflood apparatus.

A synthetic fluid composed of 89.5 mol% methane and 10.5 mol% n-heptane was selected for injection. Fluid properties, such as dew points, viscosities, condensate gas ratio (CGR), interfacial tensions, etc. were determined through equation of state (EOS) calculations. At 70 °F, the dew point and CGR were estimated to be 3,750 psia and 80 STB/MMSCF, respectively. Prior to charging into the accumulator for testing, reconditioning was performed by rocking the sample overnight at 8,000 psia and 100 °F.

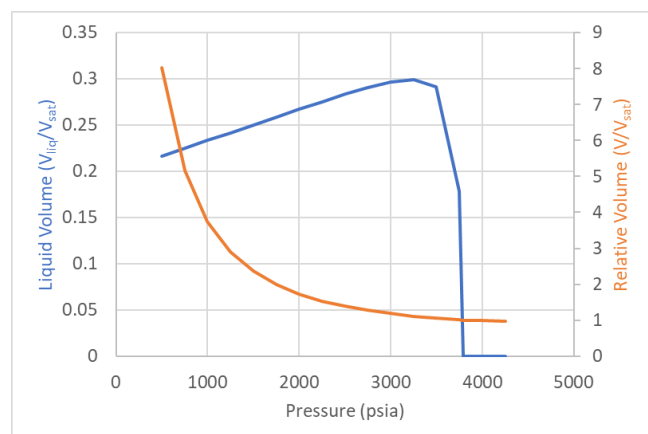


Fig. 2. Simulated Constant Composition Expansion (CCE) data at 70°F for model gas condensate (89.5 mol% methane and 10.5 mol% n-heptane) used in this study.

Tests for the 5 samples were conducted utilizing the same fluid sample. Coreflooding began by saturating the core plugs in the NMR or MRI with n-heptane followed by a permeability measurement. Next, the gas condensate was injected into sample displacing the heptane at 4000 psi. The gas condensate was injected from the source accumulator through the back pressure regulator (BPR), then into the core sample, and finally received into the receiving accumulator. Pressure drop across the sample was kept below 100 psi to reduce the impact of pressure changes on phase properties. After injecting several pore volumes (PV) and stabilization of

the differential pressure, the gas condensate permeability test performed. Tests were performed at pressures ranging from 3,500 psi to 1,000 psi in order to vary $k_{r,g}/k_{r,o}$ ratios and $N_{c,g}$ values. Pressure in the sample was decreased from one setpoint to another by reducing the pressure in the receiving accumulator over the course of 4 to 6 hours. A flow bypass remained open to ensure that there was little to no differential pressure across the core during this process. At the new pore pressure, the bypass closed and flow established through the core. Several PVs injected through the core and the differential pressures allowed to stabilize once again. The BPR located between the coreholder and the source accumulator ensured that the gas condensate fluid remained above its dew point during portions of the test while the core's pore pressure was below the fluid's dew point.

Table 1. Selected Core samples.

Core ID	Description	Porosity (v/v), NMR	Permeability (mD), Single Phase Gas Condensate
ILS	Indiana Limestone	0.17	46.8
A	Tight Sandstone	0.22	1.00
B	Tight Sandstone, very fine grain	0.10	0.02
C	mudstone, organic rich	0.03	0.002
D	Muddy, siltstone	0.08	0.0002

2.2 NMR and MRI Experiments

At each pressure step, NMR and/or MRI measurements were performed. Samples ILS, A, B, and C were performed in the 2 MHz NMR coreflood rig, while Sample D was run in the 42 MHz MRI coreflood apparatus. NMR measurements consisted of a saturation recovery Carr-Purcell-Meiboom-Gill (SR-CPMG) Pulse sequence to determine T_1 - T_2 distributions [5] with an echo spacing of 0.2 msec and recovery time ranging from 0.1 to 30,000 msec.

MRI experiments consisted of 3D Conical Single Point Ramped Imaging with T_1 Enhancement (SPRITE) Method [6]. Encoding time of 0.085 msec, repetition time of 6 msec, and 39 conical interleaves. $N_x \times N_y \times N_z$ was set to 64^3 , and the Field of View (FOV) of 54 mm in all dimensions.

3 Results and Discussion

Figures 3 and 4 display the results from the coreflood test in the five samples. Figure 3 illustrates the relationship between gas relative permeability and the dimensionless capillary number, $N_{c,g}$ while Figure 4 present the condensate relative permeability versus oil capillary number, $N_{c,o}$. Data was generated using the method proposed by Whitson et al [2] and App and Burger [4]. Once steady-flow was established

through the core, the $k_{r,g}/k_{r,o}$ relationship is determined by EOS relationships. Namely,

$$\frac{k_{r,g}}{k_{r,c}} = \left(\frac{1}{V_{r,o}} - 1 \right) \frac{\mu_g}{\mu_c} \quad (1)$$

Where $V_{r,o}$ is the relative volume determined by constant composition expansion (or EOS in this scenario), μ_g is the gas phase viscosity, μ_c the condensate viscosity, and $k_{r,g}$ and $k_{r,c}$ the gas and condensate phase relative permeabilities, respectively. After establishing the fractional flow, the relative permeabilities can be calculated.

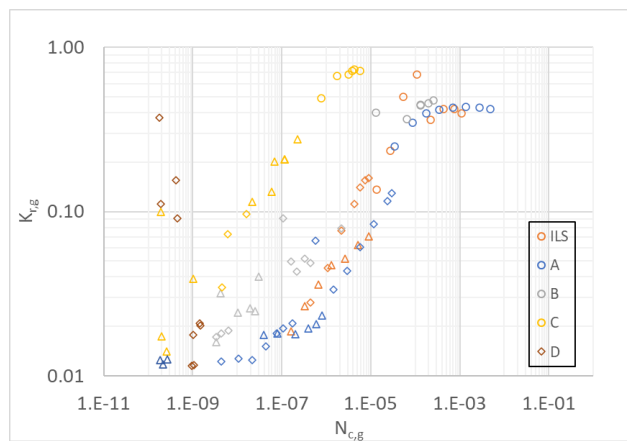


Fig. 3. Gas relative permeability ($k_{r,g}$) vs. gas capillary number ($N_{c,g}$). Triangles, diamonds, and circles represent $k_{r,g}/k_{r,o}$ values of 0.48, 0.65, and 1, respectively.

For reference purposes in trends, we compare the data collected during this study with data published in the literature [7] [8] [9] [10] [11] [12] [13] [14] in the form of $k_{r,g} = f(k_{r,g}/k_{r,o}, N_c)$ in figures 5 through 7. This form captures the relative permeability relationship linked to well deliverability in gas-condensate reservoirs [2] and it is widely used to compare data, fitting and spreadsheet calculations [1]. With the exception of [13], most of this data was measured in conventional reservoir sands and beres sandstone, and a large part was measured using synthetic mixture. For the range spanning $1 \cdot 10^{-6} \leq N_c < 5 \cdot 10^{-6}$ (Figure 5), we observe a couple of points for ILS and sample C above the previously reported values. Similarly for the range spanning $5 \cdot 10^{-6} \leq N_c < 2 \cdot 10^{-6}$ (Figure 6), we observe agreement with previously reported data with the exception of one point from ILS and one from Sample B. In the range, $N_c > 2 \cdot 10^{-6}$, good agreement is noted between the data generated in this study and previously reported data. Data from lower capillary numbers was excluded from comparison. Higher uncertainty is expected in this experimental range especially from lower permeability cores. For samples C and D, processing experimental data to yield useful information often became difficult due to low permeabilities and corresponding small pore sizes. In order to maintain below 100 psi pressure drop across the sample, pumps were often running at their lowest settings and actual flow rate through core rate was more than likely not reflected by the pump rate set point. Furthermore,

capillary pressure is neglected in this analysis which may not be realistic at smaller and smaller pore sizes.

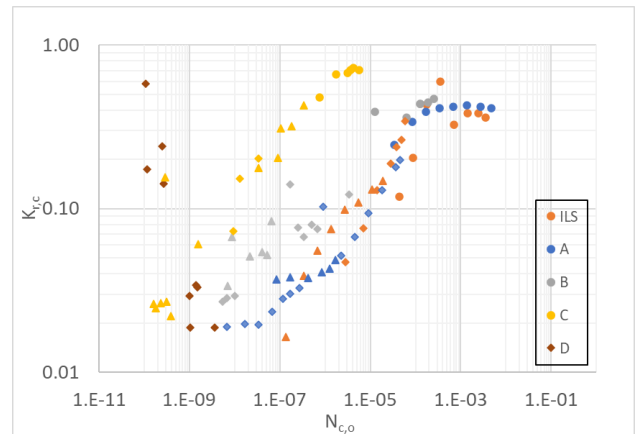


Fig. 4. Condensate relative permeability ($k_{r,c}$) vs. oil capillary number ($N_{c,o}$). Triangles, diamonds, and circles represent $k_{r,g}/k_{r,o}$ values of 0.48, 0.65, and 1, respectively.

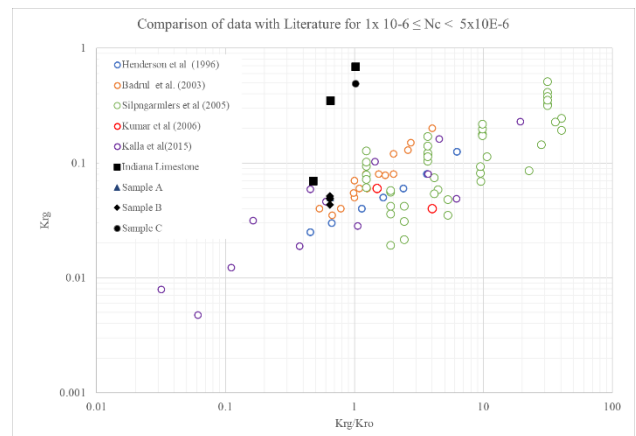


Fig. 5. Comparison of experimental data with literature results for $1 \cdot 10^{-6} \leq N_c < 5 \cdot 10^{-6}$

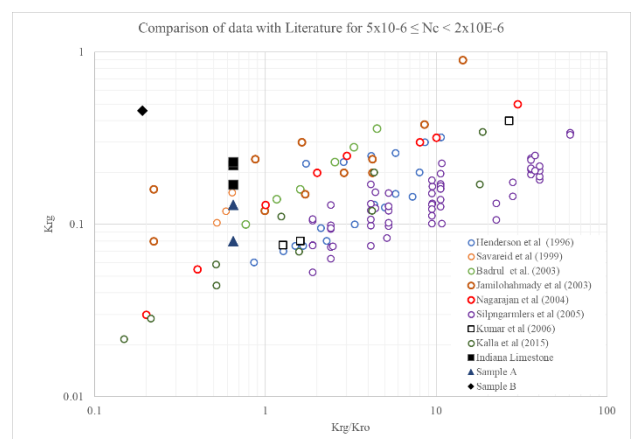


Fig. 6. Comparison of experimental data with literature results for $5 \cdot 10^{-6} \leq N_c < 2 \cdot 10^{-6}$

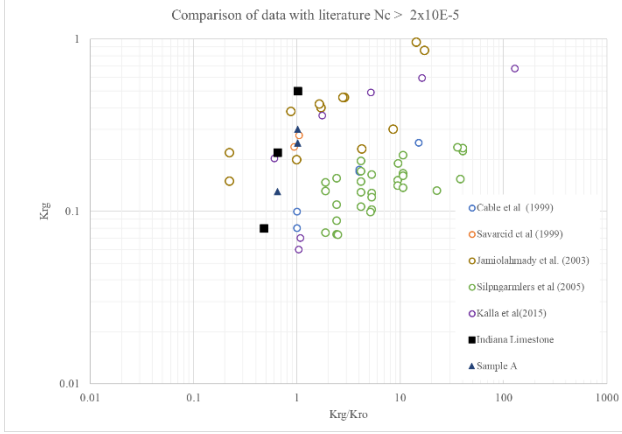


Fig. 7. Comparison of experimental data with literature results for $N_c > 2 \cdot 10^{-5}$

After establishing $k_{r,g}$ and $k_{r,o}$, the steady state relative permeabilities, an estimate of saturation can be made by fitting this data to the model presented by Whitson et al. [2]. The immiscibility factor, f_i , relates the gas phase permeability to the capillary number.

$$N_c = \frac{\mu v}{\phi(1-S_{wi})\sigma} \quad (2)$$

$$f_i = \frac{1}{(\alpha N_c)^n + 1} \quad (3)$$

$$k_{r,g} = f_i k_{r,gl} + (1 - f_i) k_{r,gM} \quad (4)$$

Where v is velocity, ϕ is porosity, σ is interfacial tension, S_{wi} is the initial water saturation, α and n are scaling factors between N_c and f_i , $k_{r,gl}$ is the immiscible gas phase relative permeability when $N_c = 0$ while $k_{r,gM}$ is the ‘miscible’ straight line gas line permeability ($N_c = \infty$). A Corey approximation [2] [15] can be used to relate the saturation to relative permeability in the immiscible, low capillary number region.

$$k_{r,g} = k_{r,g}^o \left[\frac{(1-S_{oe})(1-S_{wi}) + S_m - 1}{S_m - S_{wi}} \right]^2 \left[1 - S_{oe} \frac{\lambda_g + 2}{\lambda_g} \right] \quad (5)$$

$$k_{r,c} = k_{r,c}^o \left[\frac{S_{oe}(1-S_{wi}) - S_{oc}}{1 - S_{oc} - S_{wi}} \right] \left[S_{oe} \frac{\lambda_c + 2}{\lambda_c} \right] \quad (6)$$

Where S_o is the oil saturation, S_{wi} is the initial water saturation, S_{oc} is the critical oil saturation, $S_{oe} = S_o / (1 - S_{wi})$, S_m is 1 minus the critical nonwetting phase saturation (gas phase), λ_c and λ_g are the condensate and gas Corey exponents, respectively, and $k_{r,g}^0$ and $k_{r,c}^0$ are the relative permeability at $S_{wi} = 0$ and $S_{oe} = 1$.

Presented in Table 2 are the parameters used fitting the experimental data. S_{wi} was determined via NMR and not adjusted during the fit. The α term relates the ‘immiscible’ fraction to the capillary number and can be represented by

equation 7 where α_0 term is adjusted during fitting and $\alpha_{0,est}$ is based on rock properties and used as an initial guess

$$\alpha = \frac{\alpha_0}{k_{r,g}} \quad \text{where } \bar{k}_{r,g} = \frac{k_{r,gM} + k_{r,gl}}{2} \quad \text{and } \alpha_{0,est} = \frac{10^4}{\sqrt{k\phi}} \quad (7)$$

where k is absolute permeability in millidarcies. α_0 is dependent on properties of the rock. As permeability of these samples decreases, $\alpha_{0,est}$ increases. Similarly, $k_{r,g}$ and $k_{r,o}$ vs capillary number appears to shift to left as permeability is reduced which can be seen in the increase in the fitted α_0 term. As $\sqrt{k\phi}$ decreases over 3 orders of magnitude between samples A and C, the S-shaped curves depicting the relationship between relative permeability and capillary number undergo roughly an equivalent shift to the left in figures 3 and 4 indicating that the region over which permeabilities transition from straight line miscible permeabilities to rock dominated permeabilities shift to lower capillary numbers as $\sqrt{k\phi}$ decreases.

The inclusion of a Corey function when fitting $k_{r,g}$ and $k_{r,o}$ allows for an estimation of saturation as it becomes one of the parameters to be solved for during the fit. The results of which are presented in figure 8 and additionally, can be compared to independent measurement taken via NMR or MRI.

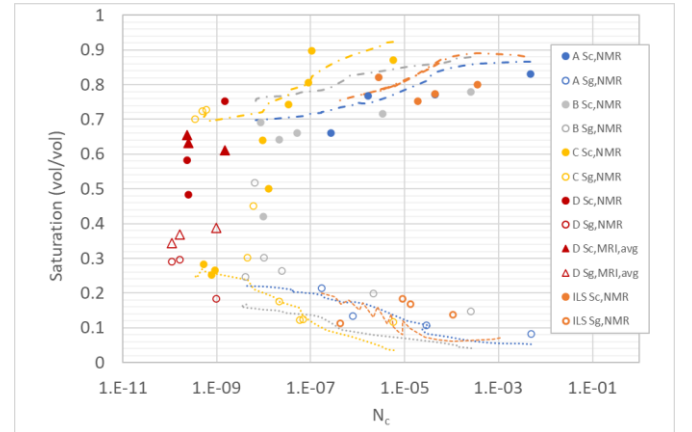


Fig. 8. Condensate (S_c) and Gas (S_g) saturations vs. capillary number ($N_{c,o}$ and $N_{c,g}$). Closed and open symbols represent condensate and gas saturations determined via NMR or MRI, respectively. Dashed and dashed-dot represent the saturation determined from model fit (see Table 2).

Table 2. Fit parameters for experimental results.

	ILS	A	B	C
$\alpha_{0,est}$	3,645	4,770	209,150	1,232,900
α_0	14,115	4,838	40,632	2,413,696
n	1.45	0.75	0.68	1.56
λ_c	0.18	0.17	0.13	0.32
λ_g	0.5	5.66	0.54	0.5
S_{oc}	0	0.1	0.15	0.04
S_{wi}	0.05	0.09	0.08	0.04

T_1 - T_2 measurements were performed throughout each coreflood. These measurements provide an alternate method for determining saturation during the coreflood. Saturations determined from the interpretation of the T_1 - T_2 maps are included in figure 8 as the open and closed symbols representing the gas and condensate saturations, respectively.

T_1 - T_2 maps are used in an effort to distinguish fluid phases: water, liquid condensate, and gas. Water was identified by comparing measurements from as-received samples to other measurements at varying capillary numbers. Fast relaxing components with T_1 - $T_2 = 1$ that remained fairly constant from test to test were taken to be an immobile aqueous phase. In the case of Sample D, two fast relaxing peaks were identified at early T_2 times. One with a T_1 - T_2 roughly of 1 was assigned to water and the other with a ratio approximately equaled to 3 attributed to oil in tight pores. For the unconventional samples (B,C, and D), data with a high T_1 - T_2 ratio was assumed to be a heavy oil or oil in organic porosity.

As the experiments progresses from one pressure to another, this has a direct impact both on the phase behavior of the fluids as well as the NMR response. Gas and condensate Hydrogen Index, HI_g and HI_c , respectively, were approximated [16] using equations 10 and 11. Densities and compositions were taken from EOS calculations, and the results are presented in figure 9.

$$HI_g = \frac{\sum_i^n \tilde{\rho}_i N_{H,i}}{0.111} \quad (10)$$

$$HI_c = \frac{\rho_m^{(R)/(12.011+1.008R)}}{0.111} \quad (11)$$

Where HI_g and HI_c are the gas and liquid condensate Hydrogen Index, respectively, $\tilde{\rho}$ is the partial molar density of species i in mol mL⁻¹, ρ_m represent the mass density in g mL⁻¹, $N_{H,i}$ represents the number hydrogen molecules per

molecule of component i , and R is the hydrogen to carbon ratio. These parameters were determined via EOS calculations.

HI values associated with the test at the lowest capillary number, typically from the test at 1,000 psi, were used to establish NMR T_1 - T_2 cutoffs for each core sample. A T_1 - T_2 cutoff was determined by matching the estimated pore volume, using the HI values for the gas and condensate phases, with the porosity of the single phase gas condensate measurement. The NMR measurements taken at the smallest capillary number were selected for determining the cutoff because each sample was at or nearest to its ‘immiscible’ state, and therefore the calculated HI values closest to their true values. This cutoff was applied to all T_1 - T_2 measurements for the same core sample made below the dewpoint for saturation determinations. Saturation determined via NMR are presented in figure 8. Examples of T_1 - T_2 are presented in figure 10 and 11.

$$PV = V_w + V_c + V_g \quad (8)$$

$$PV = \frac{1}{C} \left(M_{0,w} + \frac{M_{0,c}}{HI_c} + \frac{M_{0,g}}{HI_g} \right) \quad (9)$$

Where PV denotes the sample’s pore volume, V_i is the volume of phase i , M_0 is the initial magnetization of phase i , C is a NMR calibration factor, and the subscripts w,c , or g represent the phases: water, condensate or gas, respectively.

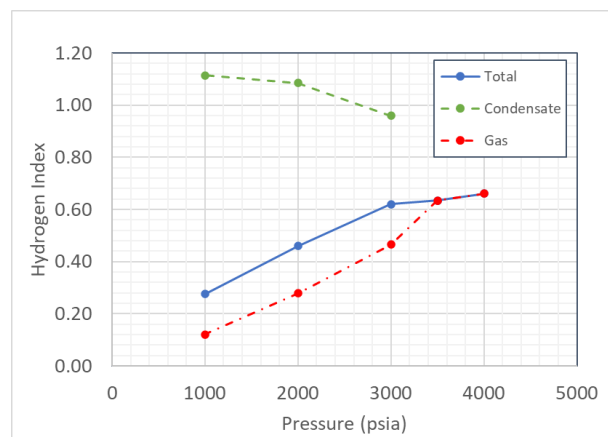


Fig. 9. Hydrogen Index (HI) of gas condensate sample at selected pressure and 70°F. Total represents the average HI weighted by the phase volumes determined by CCE calculations.

Testing for sample D was performed in a 42 MHz MRI. This allowed for imaging of the test in an effort to determine the spatial distribution of saturation. MRI SPRITE was deemed an effective method to capture the spin density distribution of the core samples at different saturation states. Since the HI of vapor and condensate differ greatly and change consistently as pressure is ramped down, spin density images were thought to contain useful information regarding the saturation state of the sample. Results from the scans are presented in figure 13. An effort to calculate gas and condensate saturation (figure 14) was made using equation 11 which uses the ratio of the signal intensities of voxel i

during a test at a given capillary number to the same voxel when saturated with the single phase gas condensate.

$$M_{0,i} = \phi_i V_i (S_{c,i} H_{Ic} + S_{g,i} H_{Ig}) \quad (10)$$

$$S_{c,i} = \frac{M_{0,i} H_{Ig,SP} - H_{Ig}}{H_{Ic} - H_{Ig}} \quad (11)$$

Where M_0 denotes the initial magnetization, p the porosity, ϕ the voxel volume, and S_c and S_g the condensate and gas saturation respectively.

Calculations via equation 11 yield a qualitative estimate of saturation. NMR and MRI results differ up to 20%. This disparity between the NMR and MRI estimates in estimation of gas and condensate saturation is noted in figure 8. For samples D, an immobile water phase is present as well as potentially oil in organic porosity. Distinguish of multiple phases with a signal MRI spin density image is optimistic at best, and additional contrast images should be considered.

Average of the condensate saturation was calculated through an arithmetic averaging of the computed voxel condensate saturations. Saturation profiles are shown in figure 12, and an overall average is represented in figure 8. For Sample D, it is clear that the saturation profile is not constant, and that there may be some impact of wettability and capillary end effects at both the inlet and outlet of the core sample resulting in a non-uniform saturation profile. Due to wetting effects, even at a low V_{ro} near the dew point, liquid is trapped in the core and it accumulates so that the saturation quickly reaches residual gas saturation. This becomes apparent with measurement of saturation profile of sample D using MRI.

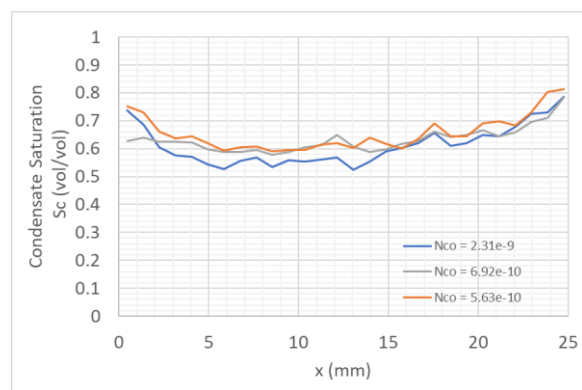


Fig. 12. Computed saturation profile from results in figure 14.

Extreme values represented as bright white spots in the MRI-derived saturation distribution (figure 14, $N_{c,o} = 2.3 \cdot 10^{-9}$ or $N_{c,o} = 5.6 \cdot 10^{-10}$) are attributed to Gibbs ringing [17] that appear to be present in the original SPRITE images. Adjustments in the FOV or matrix dimensions may help to reduce.

SPRITE imaging allows for the fast MR signal detection that enables capture of the fast relaxing components. However, in this study, only a single encoding time was used. Adjustments of encoding time for SPRITE imaging adjusts T_2^* contrast which may not improve contrast between phases. However, combined with another technique, such as T_1 [18] or T_2 profiling [19] [20], more advanced discrimination and identification of phases could be potentially performed.

5 Conclusion

In this study, we presented the gas condensate relative permeabilities measured for a selection of samples with an absolute permeability spanning from 50 to 0.0002 mD. This battery of tests allowed for capillary numbers to range from 10^{-2} to nearly 10^{-11} . For the range of capillary numbers covered in previous experimental studies, good agreement was observed between for the data collected in this study and data from previous studies. As the range in capillary number is extended to lower values and beyond previous studies, the uncertainty in the measurements increased and agreement with previous results decreased. Opportunity exists for future work to exist to further explore this region of lower capillary number, the impact of different rock and fluid types, and improve experimental methods.

NMR and MRI measurements supplemented the coreflood testing allowing for the determination of saturation during the test. NMR and MRI are strong tools for saturation analysis, but in this study discrimination between phases proved challenging. Further work is need to provide robust average and spatial realized measures of saturation including more robust EOS model that allows for accurate determination of HI during the miscible portion of the displacement would improve precision of the technique. Additionally alternative NMR or MR methods and techniques could be considered such as a partitioning component or application of diffusion weighting that impact MR signal to improve phase tracking.

6 Acknowledgements

The authors would like to thank Chevron North America Exploration and Production Company (a Chevron U.S.A. Inc division), Chevron Canada Limited, and KUFPEC Canada Inc. for their support and permission to publish this study.

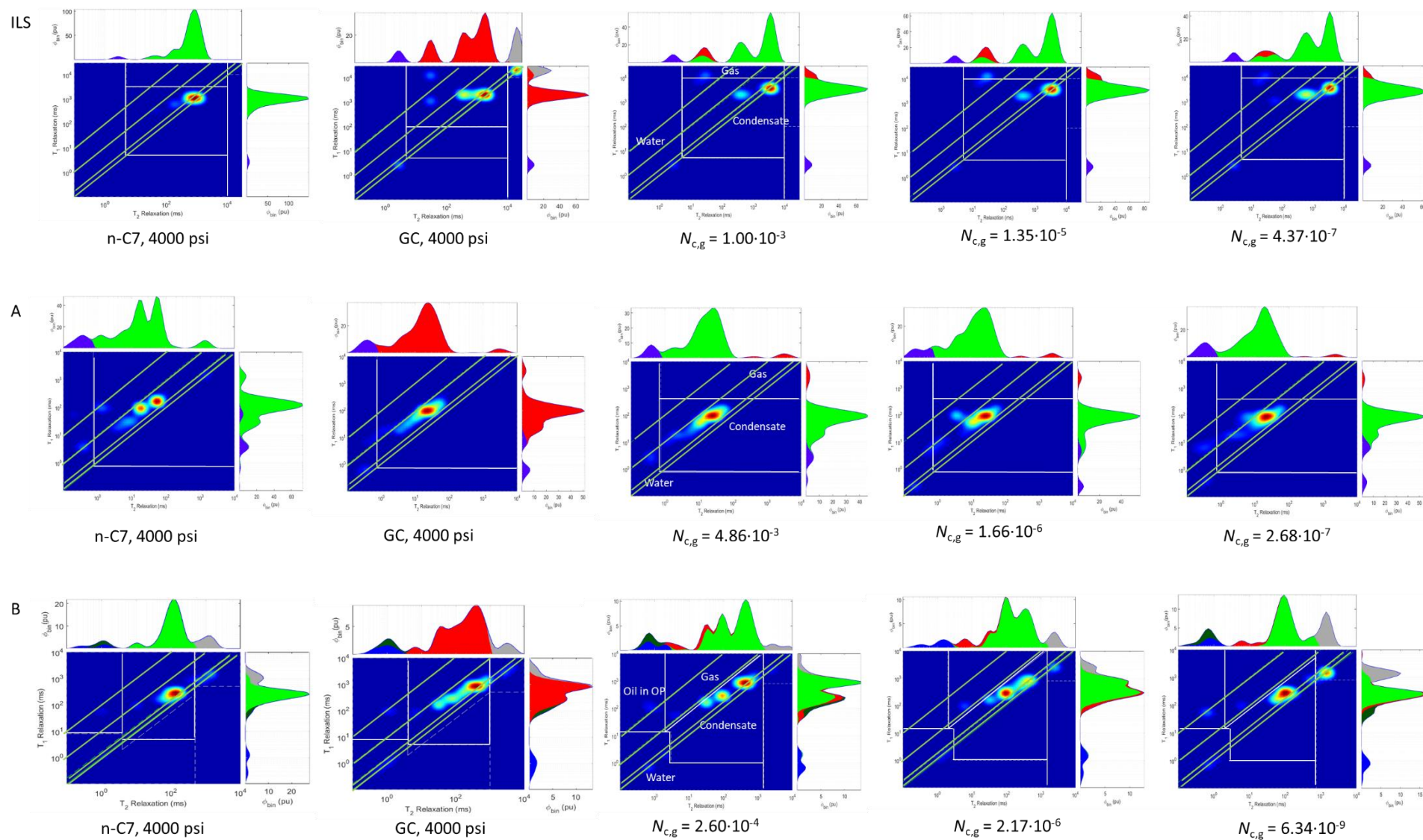


Fig. 10. Selected T_1 - T_2 distributions for samples ILS, A, and B at various experimental conditions. Green lines represent $T_1/T_2 = 1, 1.6, 10,$ and 100 . White lines denote cut-offs used to distinguish between various phases.

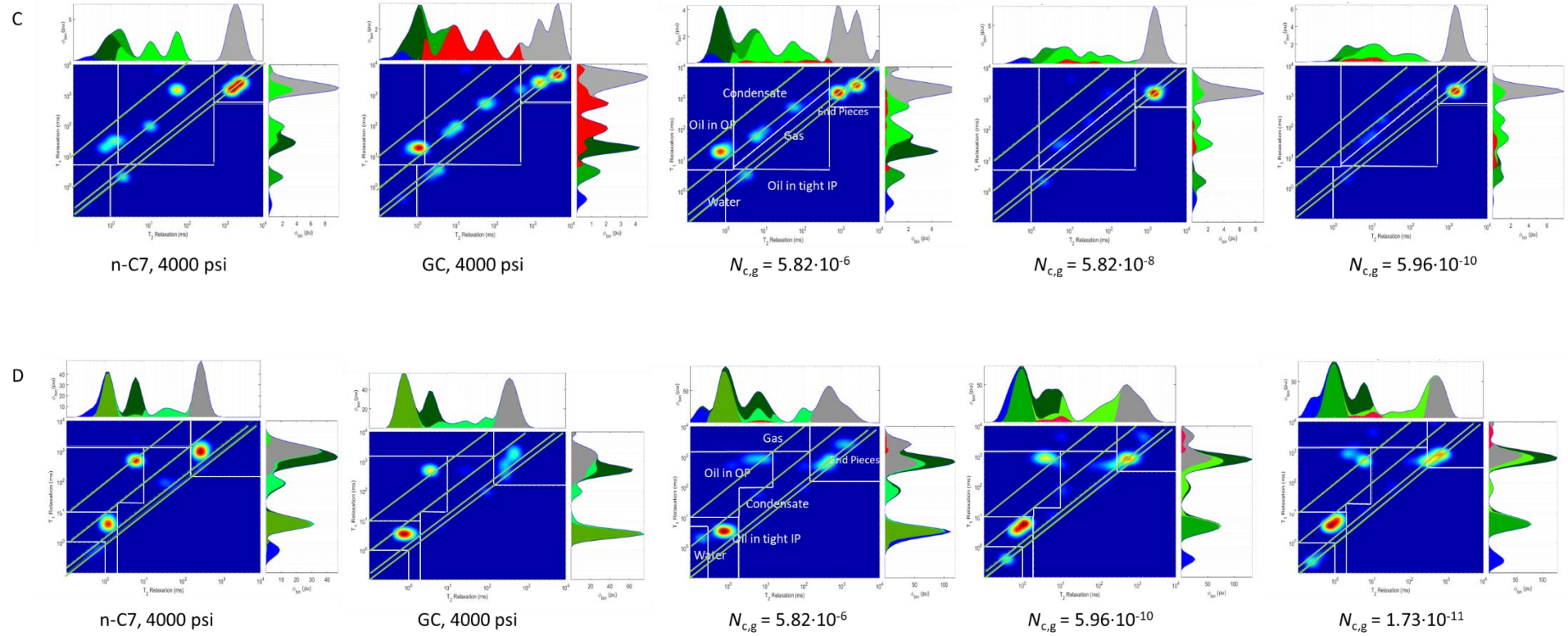


Fig. 11. Selected T_1 - T_2 distributions for samples C and D at various experimental conditions. Green lines represent $T_1/T_2 = 1, 1.6, 10,$ and 100 . White lines denote cut-offs used to distinguish between various phases.

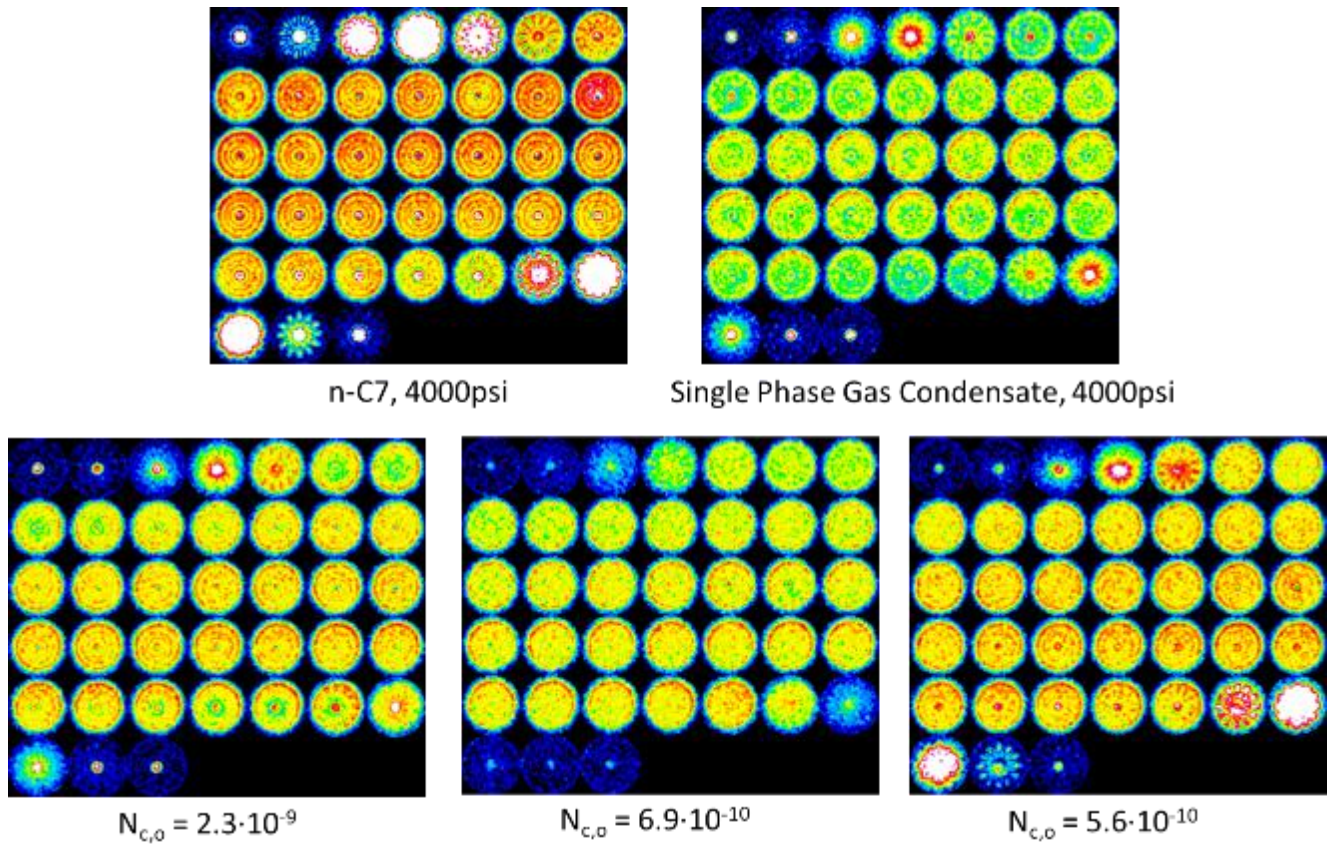


Fig. 13. MRI SPRITE Images of Sample D taken at indicated conditions.

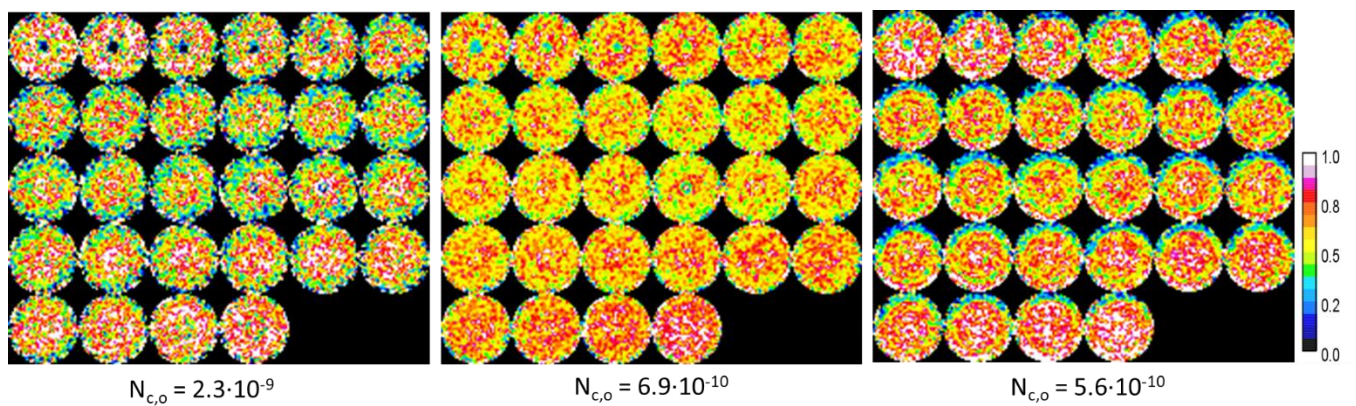


Fig. 14. Estimate of condensate saturations from SPRITE images (figure 13) using equation 11.

References

- [1] J. Kamath, "Deliverability of Gas-Condensate Reservoirs — Field Experiences and Prediction Techniques," *Journal of Petroleum Technology*, vol. 59, no. 4, pp. 94-99, 2007.
- [2] C. H. Whitson, F. Øivind and A. Sævareid, "Gas Condensate Relative Permeabilities for Well Calculations," in *SPE Annual Technical Conference and Exhibition*, Houston, TX, 1999.
- [3] K. -J. Dunn, D. J. Bergman and G. A. LaTorraca, *Nuclear Magnetic Resonance: Petrophysical and Logging Applications*, Pergamon, 2002.
- [4] J. F. App and J. E. Burger, "Experimental Determination of Relative Permeabilities for Rich Gas Condensate System Using Live Fluid," *SPE Reservoir Evaluation*, vol. 12, no. 2, pp. 263-269, 2009.
- [5] B. Sun and K.-J. Dunn, "Two-dimensional nuclear magnetic resonance petrophysics," *Magnetic Resonance Imaging*, vol. 23, no. 2, pp. 259-262, 2005.
- [6] M. Halse, D. J. Goodyear, B. MacMillian, P. Szomolanyi, D. Matheson and B. J. Balcom, "Centric Scan SPRITE Magnetic Resonance Imaging," *Journal of Magnetic Resonance*, vol. 165, pp. 219-229, 2003.
- [7] M. J. Badrul, W. S. Ucok and L. L. Robert, "Effect of Permeability Distribution and Interfacial Tension on Gas Condensate Relative Permeability: An Experimental Study," in *SPE Asia Pacific Oil and Gas Conference and Exhibition*, Jakarta, Indonesia, 2003.
- [8] A. Cable, R. Mott and M. Spearing, "Experimental Techniques for the Measurement of Relative Permeability and In-Situ Saturation in Gas Condensate Near Wellbore and Drainage Studies," in *Proceedings of International Symposium of the Society of Core Analysts*, Golden, CO, 1999.
- [9] G. D. Henderson, A. Danesh, D. H. Tehrani, S. Al-Shaidi and J. M. Peden, "Measurements and Correlation of Gas Condensate Relative Permeability by the Steady-State Method," *SPE Journal*, vol. 1, no. 2, pp. 191-201, 1996.
- [10] M. Jamiolahmady, A. Danesh, G. Henderson and D. Tehrani, "Variations of Gas-Condensate Relative Permeability with Production Rate at Near Wellbore Conditions: A General Correlation," in *SPE Offshore Europe Conference*, Aberdeen, UK, 2003.
- [11] S. Kalla, S. Leonardi, D. W. Berry, L. D. Poore, H. Sahoo, R. A. Kudva and E. M. Braun, "Factors That Affect Gas-Condensate Relative Permeability," *SPE Reservoir Evaluation and Engineering*, vol. 18, no. 1, pp. 5-10, 2015.
- [12] V. Kumar, G. A. Pope and M. M. Sharma, "Improving the Gas and Condensate Relative Permeability Using Chemical Treatments," in *SPE Gas Technology Symposium*, Calgary, Alberta, Canada, 2006.
- [13] A. Sævareid, C. H. Whitson and Ø. Fevang, "An Engineering Approach to Measuring and Modeling Gas Condensate Relative Permeabilities," in *International Symposium of the Society of Core Analysts*, Golden, CO, 1999.
- [14] N. R. Nagarajan, M. M. Honarpour and K. Sampath, "Comparison of Gas-Condensate Relative Permeability using live fluid vs. Model Fluids," in *International Symposium of the Society of Core Analysts*, Abu Dhabi, UAE, 2004.
- [15] M. B. Standing, "Notes on Relative Permeability Relationships," The Norgian Institute of Technology, The University of Trondheim, Trondheim, Norway, 1975.
- [16] G. J. Hirasaki and K. K. Mohanty, "Fluid-Rock Characterization and Interactions in NMR Well Logging," U.S. Department of Energy Office of Scientific and Technical Information, Tulsa, OK (United States), 2003.
- [17] Z.-P. Liang and P. C. Lauterbur, *Principles of Magnetic Resonance Imaging: A Signal Processing Perspective*, New York: Wiley-IEEE Press, 2000.
- [18] M. S. Zamiri, F. Marica, L. Romero-Zerón and B. J. Balcom, "Monitoring Shale Water Uptake using 2D Magnetic Resonance Relaxation Correlation and SPRITE MRI," *Chemical Engineering Journal*, vol. 428, no. 15, 2022.
- [19] M. T. Rauschhuber and G. J. Hirasaki, "Determination of Saturation Profiles via Low-Field NMR Imaging," in *Proceedings of the International Symposium of the Society of Core Analysts*, Noordwijk, The Netherlands, 2009.
- [20] O. V. Petrov, G. Ersland and B. J. Balcom, "T2 Distribution Mapping Profiles with Phase-Encode MRI," *Journal of Magnetic Resonance*, vol. 209, no. 1, pp. 39-46, 2011.